# A shape memory polymer concrete crack closure system activated by electrical current



OPEN ACCESS
IOP Publishing
Smart Materials and Structures
Smart Mater. Struct. **27** (2018) 075016 (12pp)
https://doi.org/10.1088/1361-665X/aac28a

# A shape memory polymer concrete crack closure system activated by electrical current

**Oliver Teall[1,4], Martins Pilegis[2], Robert Davies[2], John Sweeney[3], Tony Jefferson[2], Robert Lark[2] and Diane Gardner[2]**

[1] Costain Group PLC., Costain House, Vanwall Business Park, Maidenhead, Berkshire SL6 4UB, United Kingdom
[2] Cardiff University School of Engineering, Queen's Buildings, 14-17 The Parade, Cardiff CF24 3AA, United Kingdom
[3] Bradford University School of Engineering, Bradford, West Yorkshire BD7 1DP, United Kingdom

E-mail: Oliver.Teall@Costain.com

Received 10 February 2018, revised 1 May 2018
Accepted for publication 4 May 2018
Published 31 May 2018

**Abstract**

The presence of cracks has a negative impact on the durability of concrete by providing paths for corrosive materials to the embedded steel reinforcement. Cracks in concrete can be closed using shape memory polymers (SMP) which produce a compressive stress across the crack faces. This stress has been previously found to enhance the load recovery associated with autogenous self-healing. This paper details the experiments undertaken to incorporate SMP tendons containing polyethylene terephthalate (PET) filaments into reinforced and unreinforced 500 × 100 × 100 mm structural concrete beam samples. These tendons are activated via an electrical supply using a nickel-chrome resistance wire heating system. The set-up, methodology and results of restrained shrinkage stress and crack closure experiments are explained. Crack closure of up to 85% in unreinforced beams and 26%–39% in reinforced beams is measured using crack-mouth opening displacement, microscope and digital image correlation equipment. Conclusions are made as to the effectiveness of the system and its potential for application within industry.

Keywords: shape memory polymer, self-healing concrete, durability, concrete

(Some figures may appear in colour only in the online journal)

## 1. Introduction

Cracking in reinforced concrete structures is a common phenomenon, with a variety of causes. It is generally accepted that the presence of cracks has a negative impact on the durability of concrete by providing paths for corrosive materials to the embedded steel reinforcement (Van Breugel 2007, Van den Heede *et al* 2014).

Concrete is capable of natural or 'autogenous' healing in certain conditions. The width of the crack is a fundamental factor which affects the self-healing process (De Rooij *et al* 2013). Methods to restrict crack widths within concrete commonly include the introduction of steel or polymer fibres. Steel cord fibres have been found to corrode within concrete cracks, making them less effective as a crack control mechanism for self-healing purposes (Homma *et al* 2009).

Engineered cementitious composite (ECC) materials contain polymer fibres, typically 2% by volume, which help to reduce the appearance of single cracks and distribute any micro-cracks throughout the material, resulting in a smaller average crack

[4] Author to whom any correspondence should be addressed.

width compared to concrete reinforced with conventional steel bars. ECC can be designed to reduce average crack widths to as low as 0.03 mm (Li *et al* 1998, Yang *et al* 2009, De Rooij *et al* 2013).

However, A typical ECC mix contains 570 kg m$^{-3}$ portland cement and 684 kg m$^{-3}$ pulverised fly ash (De Rooij *et al* 2013), high proportions compared to conventional reinforced concrete. While contributing to self-healing by ongoing hydration, this results in a higher level of embodied $CO_2$ and increased material cost compared to more conventional mixes. Given the UK government's aim, set out in 'Construction 2025' (Government 2013), to achieve a 50% reduction in greenhouse gas emissions and 33% lower initial construction costs in the built environment by 2025, a solution which produces the same benefits as ECC while reducing the cement content would be desirable.

The application of a compressive stress across the crack faces has been shown to improve strength recovery with autogenous healing (Neville 2012). Heide and Schlangen (2007) investigated the autogenous healing of submerged concrete samples subjected to an applied compressive stress following three-point bending to induce cracks. They found that with a compressive stress of 1 N mm$^{-2}$ on the crack face, the stiffness and strength of the concrete specimen was recovered, while without this stress the strength recovery was minor.

Shape memory polymers (SMP) have been proposed as a method to apply this compressive stress within concrete structures (Jefferson *et al* 2010, Isaacs *et al* 2013). SMP are materials which respond to external stimuli by altering their physical shapes. The most common SMP are thermoresponsive, with direct heat used as the stimulus for shape change (Xie 2011). If an amorphous SMP, which has previously been oriented by drawing, is heated above its glass transition temperature ($T_g$) while restrained, a restrained shrinkage stress is produced which can be utilised to close cracks in concrete.

Over the last decade, potential biomedical applications have contributed to a large increase in SMP interest, examples of which include active medical devices such as a laser-activated device for the mechanical removal of blood clots (Xie 2011, Behl and Lendlein 2007). However, uses for SMPs have also been found in a wide range of other areas, such as smart textiles, high performance water vapour permeability materials, heat shrinkable electronics packaging, sensors and actuators, self-deployable structures in spacecraft and micro-systems (solution, emulsion, film, foam and bulk) (Meng and Hu 2009).

Proof of concept experiments carried out by Jefferson *et al* (2010) and Isaacs *et al* (2013) used drawn polyethylene terephthalate (PET) tape to close cracks in prismatic hollow mortar beam specimens, making use of the shrinkage stress generated by the material's retraction upon heating. Commercially available PET *shrink tite* samples were placed within prismatic hollow mortar beam samples, 25 × 25 × 150 mm in dimension with a 10 × 10 mm void running through the centre. The mix contained water:cement:sand contents of 306 kg m$^{-3}$:510 kg m$^{-3}$:1530 kg m$^{-3}$ (or 0.6:1:3 by weight). Layers of strips, with a total cross-sectional area of 20.7 mm$^2$, were placed through the void and externally anchored. A three-stage test was carried out, consisting of three-point loading to form a 0.3 mm width crack, dry heating in an oven at 90 °C to activate the PET specimens and a second round of three-point loading to failure. Conclusions from these tests were that activation of the tendons closed the cracks and applied a prestress of between 1.5 and 2 MPa on the mortar beam specimens (Jefferson *et al* 2010).

However, these experiments were carried out at a small scale within a laboratory setting, and use mortar beams rather than structural concrete. As suggested by Isaacs (2011), larger specimens may require polymers which generate larger shrinkage stresses for lower concrete volume replacement. A suitable activation technique for the polymers is also required. Jefferson *et al* (2010) suggest that the use of ovens to activate the PET shrink tite is regarded as a temporary solution by stating that 'It is envisaged that in later versions of the system, activation will be achieved via an electrical supply'.

This paper describes the experimental work undertaken to incorporate SMP tendons, made from bundled PET filaments, into 500 × 100 × 100 mm structural concrete beams. The beams were cracked in three-point bending and the tendons activated via an electrical current using a resistance wire heating system. Crack closure was measured using a crack-mouth opening displacement (CMOD) gauge and microscope images, with digital image correlation (DIC) used for qualitative confirmation. Testing undertaken to determine the restrained shrinkage stress generated by the filaments is described in detail in a previous paper by the author (Teall *et al* 2017).

The experiments in this paper demonstrate the feasibility of a SMP concrete crack closure system activated by electrical current, a novel approach to reducing the width of concrete cracks which has not previously been described.

## 2. PET tendons

The PET tendons are shown in figure 1 below. Each tendon was 400 mm in length and contained 200 PET filaments. The filaments were manufactured at Bradford University using a commercial grade of PET (Dow Lighter C93). The manufacturing and die-drawing process for the filaments is described in detail in Teall *et al* (2017). The final diameter of the filaments was 0.9 mm, with a draw ratio of 4.0.

To form the tendons, the filaments were wound around two pegs on a bespoke steel rig, the schematic for which is shown in figure 2. M10 (10 mm diameter) stainless steel wire rope clips were used to grip the filaments at either end (figure 3) and an injection-moulded polylactic acid (PLA) sleeve placed around the tendon to de-bond and protect the filaments from the surrounding concrete. A steel plate was placed between the wire rope clip and the sleeve. The area of the plate extended beyond the edge of the PLA sleeve to provide a flat surface to transfer the compressive stress from the tendon to the concrete, and from the tendon to the testing rig during the restrained shrinkage tests.

PTFE-coated nickel-chrome (nichrome) wire was wrapped around the filaments to provide the heat for activation when passing a current through the wire. The PET filaments were coated in silicone grease to improve heat transfer. A coil

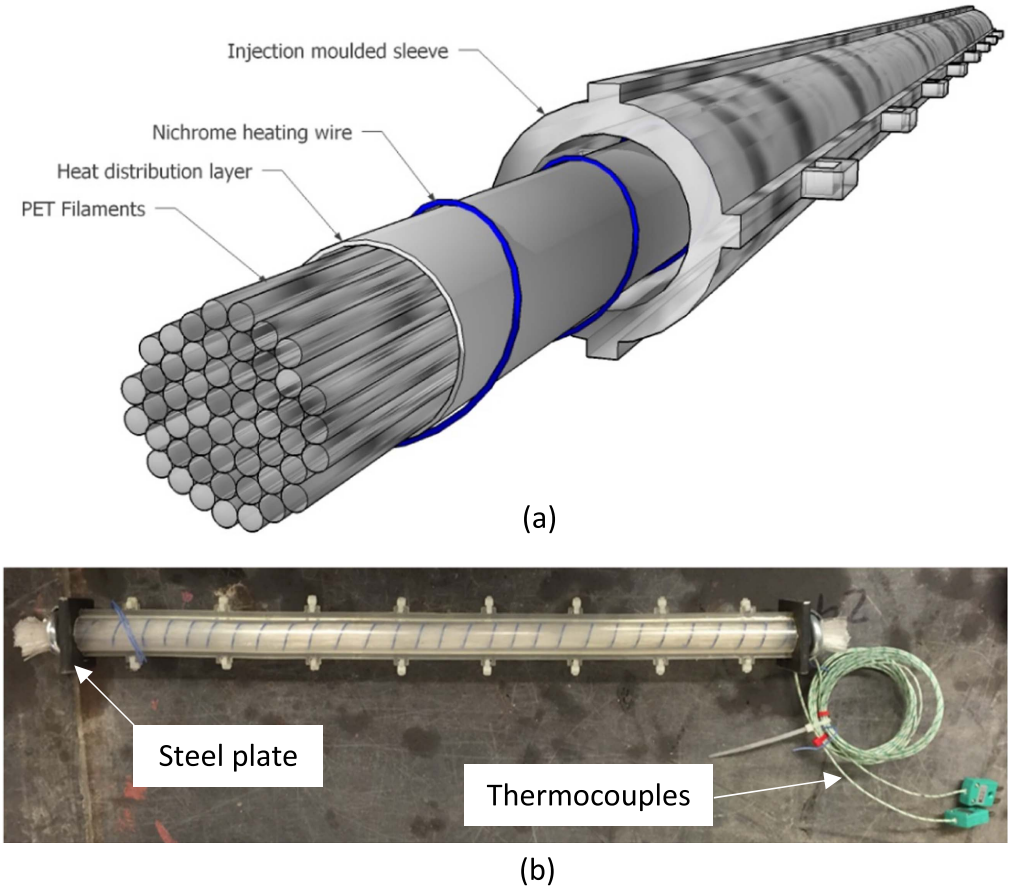


**Figure 1.** Shape memory PET tendon concrete crack closure system (a) schematic (b) photo.

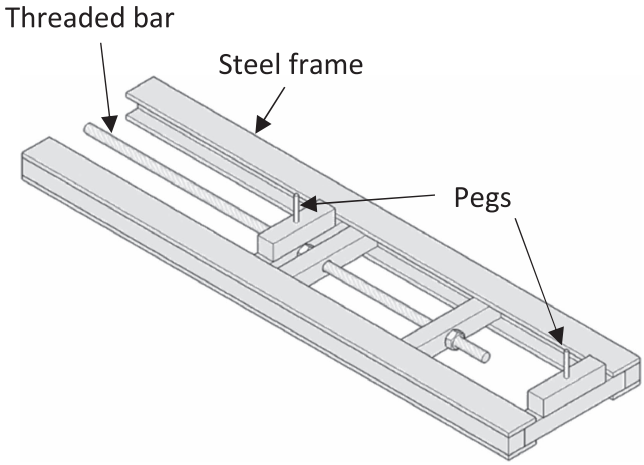


**Figure 2.** Schematic of bespoke steel rig for making filament tendons.

spacing of 10 mm was used for the nichrome wires. Two thermocouples were incorporated into each tendon, as shown in figure 4, to measure temperature during activation. The first, 'internal' thermocouple was placed near the centre of the filament bundle. The second 'external' thermocouple was placed on the surface of the filaments, between two heating coils.

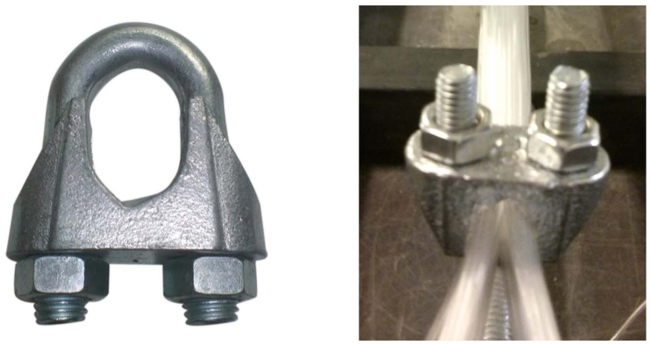


**Figure 3.** (a) Wire rope clips; (b) wire rope clip on PET filaments.

## 3. Experiment set-up

### *3.1. Restrained shrinkage test*

To test the restrained shrinkage stress produced by each tendon, they were placed within a steel grip arrangement as shown in figure 5. The steel grips were connected by a threaded bar and nut to a 5 kN full bridge strain gauge to measure load. The steel plates at either end of the tendon rested on the steel grips, providing a surface for transferring load. Before testing, the tendons were loaded to a pre-stress of 2 MPa by increasing the distance between the two steel grips

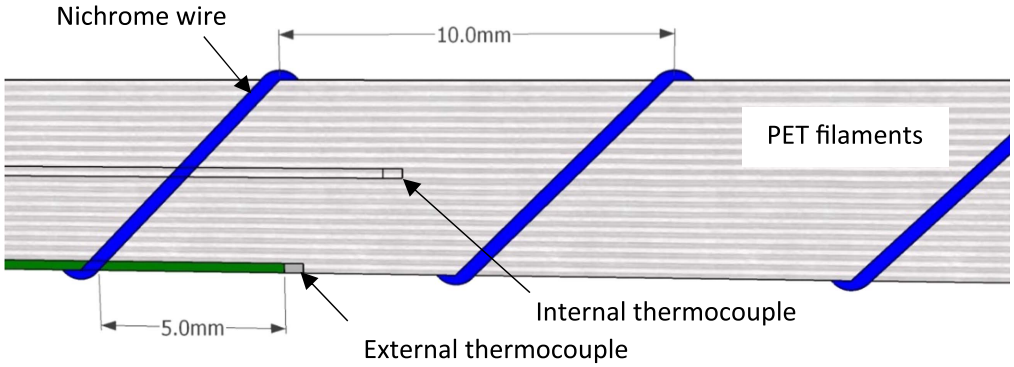


**Figure 4.** Position of thermocouples within PET filament tendon.

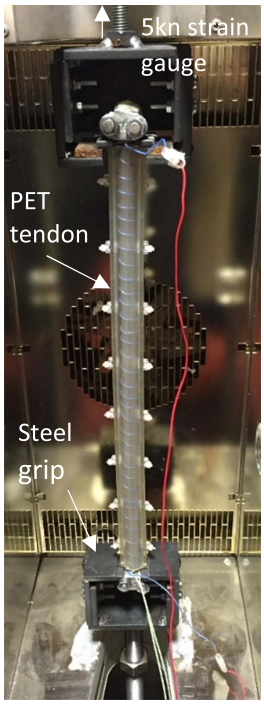


**Figure 5.** Shape memory PET tendon testing rig arrangement.

using the threaded bar. Each end of the nichrome heating wire was connected to a length of low-resistance copper wire, which was in turn attached to an Ashley-Edison AE-130-LB variable transformer connected to a 230 V mains supply, allowing the input voltage to be manually varied.

### *3.2. Concrete crack closure tests*

The concrete beam samples measured 500 × 100 × 100 mm and were cast using steel moulds. Each of the test beams contained one PET tendon. The reinforced samples also contained two 6 mm diameter high tensile ribbed steel bars. The set-up of the reinforced samples prior to casting is shown in figure 6 and the cross-sections of unreinforced and reinforced beam samples are shown in figure 7.

The concrete mix design shown in table 1 was mixed using a Belle Premier 200XT mixer and compacted in three layers on a vibrating table. Coarse aggregate consisted of 4–10 mm diameter limestone. Fine aggregate used was

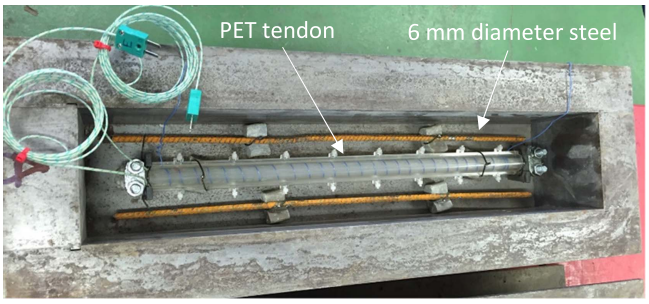


**Figure 6.** Reinforced test sample set-up prior to casting.

0–4 mm diameter natural sea-dredged sand from Swansea Wharf and 0–2 mm diameter limestone dust sieved from 0–4 mm diameter limestone aggregates. All of the limestone was sourced from Cornelly Drystone Quarry in Porthcawl, South Wales. The cement used was CEM II/B-V 32, 5R with 21%–35% Fly Ash content, consistent with BS EN 197-1 classifications. This was sourced from Lafarge Tarmac.

The target consistency of the fresh concrete, measured using the slump test to BS EN 206:2013 (BSI 2013), was S3 (100–150 mm). Adomast Adoflow Extra plasticiser was added to the mix after all other constituents to reach the target slump range, in amounts not exceeding 1.75 kg $m^{-3}$.

After air-curing for 24 h, the specimens were submerged in water at 20 °C for 5 d. They were then removed from the water, a 5 mm deep notch was cut as a crack-inducer at mid-span and knife edges attached to measure CMOD. The beams were left for a further 24 h to dry in ambient conditions, before testing at 7 d after casting. The beam sample references and descriptions are given in table 2 and the full testing methodology described in table 3.

## 4. Experimental methodology

### *4.1. Restrained shrinkage test*

The input voltage was raised until 90 °C was recorded on the internal thermocouple. The temperature was then regulated by manually switching the system on and off to keep the reading within 5 °C of this target temperature for 15 min. This caused the temperature measured by the external thermocouple to fluctuate between 80 °C and 90 °C due to a higher rate of heat

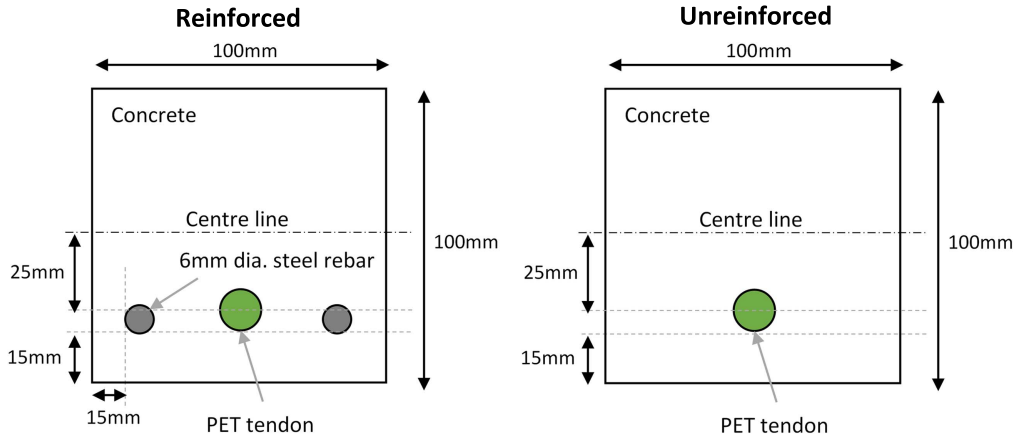


**Figure 7.** Cross-section of reinforced and unreinforced test beams.

**Table 1.** Nominal concrete mix design (saturated surface dry quantities).

| Cement (kg m$^{-3}$) | $w/c$ ratio | Coarse aggregate (kg m$^{-3}$) | Fine aggregate (kg m$^{-3}$) | Limestone dust (kg m$^{-3}$) | Water (kg m$^{-3}$) | Admixture (kg m$^{-3}$) |
|---|---|---|---|---|---|---|
| 400 | 0.48 | 990 | 648 | 162 | 192[a] | 1.75[b] |

[a] Nominal SSD quantity, actual added water adjusted according to aggregate water content.
[b] Plasticiser was added to reach the target slump range in amounts not exceeding 1.75 kg m$^{-3}$.

**Table 2.** Specimen descriptions.

| Sample | Series | Description |
|---|---|---|
| PET A | Unreinforced | 500 × 100 × 100 mm concrete beam containing 1 PET tendon |
| PET B | Unreinforced | 500 × 100 × 100 mm concrete beam containing 1 PET tendon |
| PET C | Unreinforced | 500 × 100 × 100 mm concrete beam containing 1 PET tendon |
| Control (x3) | Unreinforced | 500 × 100 × 100 mm concrete beam |
| PET A-r | Reinforced | 500 × 100 × 100 mm concrete beam containing 1 PET tendon and 2 no. 6 mm diameter high tensile steel bars |
| PET B-r | Reinforced | 500 × 100 × 100 mm concrete beam containing 1 PET tendon and 2 no. 6 mm diameter high tensile steel bars |
| PET C-r | Reinforced | 500 × 100 × 100 mm concrete beam containing 1 PET tendon and 2 no. 6 mm diameter high tensile steel bars |
| CONT A-r | Reinforced | 500 × 100 × 100 mm concrete beam containing 2 no. 6 mm diameter high tensile steel bars |
| CONT B-r | Reinforced | 500 × 100 × 100 mm concrete beam containing 2 no. 6 mm diameter high tensile steel bars |
| CONT C-r | Reinforced | 500 × 100 × 100 mm concrete beam containing 2 no. 6 mm diameter high tensile steel bars |
| Cubes (x6) | Unreinforced and reinforced | 100 × 100 × 100 mm cube samples for compression tests |

loss on the external face of the tendon. The electricity supply was then turned off, allowing the tendon to cool to room temperature. The load and temperature were measured at a rate of 2 Hz using the load cell and thermocouples respectively. This test was repeated with three tendons.

### *4.2. Concrete crack closure tests*

Table 3 describes the testing methodology for the PET tendon in unreinforced and reinforced beam samples. Cube samples were also tested at 7 and 28 d for compressive strength. The three-point bending set-up is shown in figure 8.

### *4.3. Crack width and strain measurements*

Images of the cracks were taken on both sides of the beam samples using a Veho Discovery VMS-001 USB microscope along with a graduated scale. Images were taken at peak load and after unloading on both the initial and reload cycles. Additional images were taken immediately after activation of the tendon. From each image, three crack width measurements 0.75 mm apart were made perpendicular to the crack face using ImageJ software (Schneider *et al* 2012), as illustrated in figure 9. Average crack width measurements from both sides of the beam were used for comparison.

Displacement and strain were also measured using a DIC system, consisting of two LaVision Imager X-lite 8 M CCD

**Table 3.** Testing methodology for PET tendons in unreinforced and reinforced beam samples.

| Day from casting | Action | Description |
|---|---|---|
| 0 | Casting of all beams | Beams cast and left to cure in air |
| 1 | Submersion | Beams removed from steel moulds and submerged in water at 20 °C |
| 6 | Preparation for testing | Removal from water, given 5 mm notch and knife edges |
| 7 | Initial three-point bend testing of all beams | Unreinforced beams (PET A-C and controls)<br>Loaded to 0.5 mm CMOD at a rate of 0.001 mm $s^{-1}$ (CMOD controlled). At 0.5 mm the CMOD was held constant while microscope images were taken of both sides of the beam (at crack location). The beams were then unloaded and additional microscope images taken<br>Reinforced beams (PET A-r, B-r, C-r and CONT A-r, B-r, C-r)<br>Loaded to 15 kN at a rate of 0.001 mm $s^{-1}$ (CMOD controlled). At 15 kN the CMOD was held constant while microscope images were taken of both sides of the beam (at crack location). The beams were then unloaded and additional microscope images taken. |
| 7 | Activation of PET tendons | Immediately after initial testing, the tendons were activated by passing a current through the nichrome wire. The voltage was increased until either a temperature plateau of 90 °C was reached on the internal thermocouple, or the wire temperature reached 150 °C[a]. This voltage was then kept constant for 1 h[b] before turning off the electricity supply and allowing the tendon to cool to room temperature.<br>Cont B-r was also left for an hour as a control to test the effect of the reinforcing steel on the gradual crack closure over this time period |
| 7 | Retesting of beams in three-point bending | Unreinforced beams (PET A-C)<br>Reloaded to 1 mm CMOD at a rate of 0.001 mm $s^{-1}$, additional microscope images taken, then unloaded<br>Reinforced beams (PET A-r, B-r, C-r and CONT A-r, B-r, C-r)<br>Reloaded to 15 kN at a rate of 0.001 mm $s^{-1}$, additional microscope images taken, then unloaded. For PET A-r, PET C-r and Cont B-r two additional reloads were completed to investigate the cyclic loading effect. Cont A-r was also reloaded a second time before a machine error caused the failure of the beam. Cont C-r was only reloaded once |

[a] A separate study on the activation system showed that the temperature on the outside of the sleeve temperature never exceeded 100°C and from this study it is was concluded that the heating of the tendon would not cause any damage to the surrounding concrete matrix.
[b] The temperature was not regulated as the thermocouple readings reached a plateau using voltage control alone.

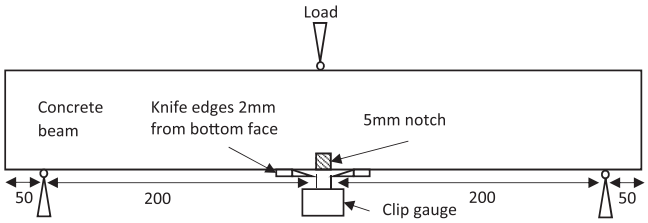


**Figure 8.** Three-point bend test set-up (dimensions in mm).

cameras and DaVis analysis software. A speckle pattern (to create unique subsets) was painted (using spray paint) on to the side of all beams containing PET tendons and one control beam from both the unreinforced and reinforced beam series. A typical example of this pattern is shown in figure 10. Images were taken every 30 s during loading, activation and reloading using the DIC system. These images were then

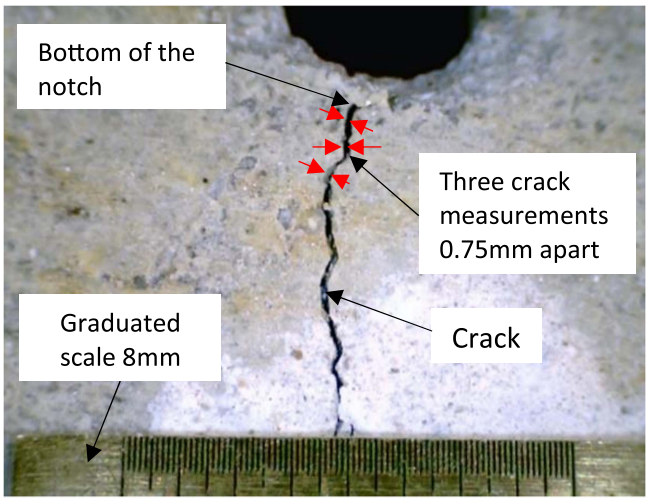


**Figure 9.** Crack measurement using microscope.

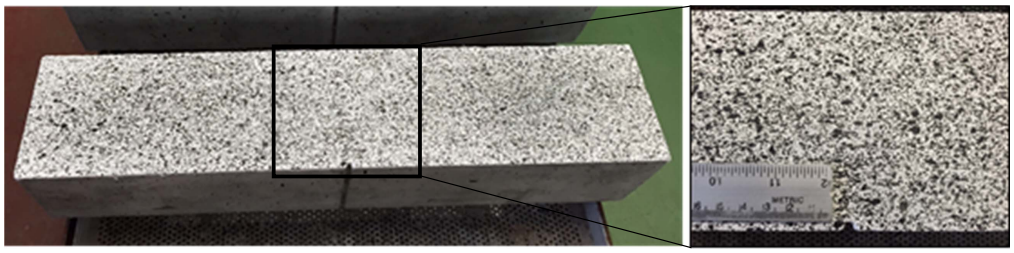

**Figure 10.** Applied speckle pattern for DIC system.

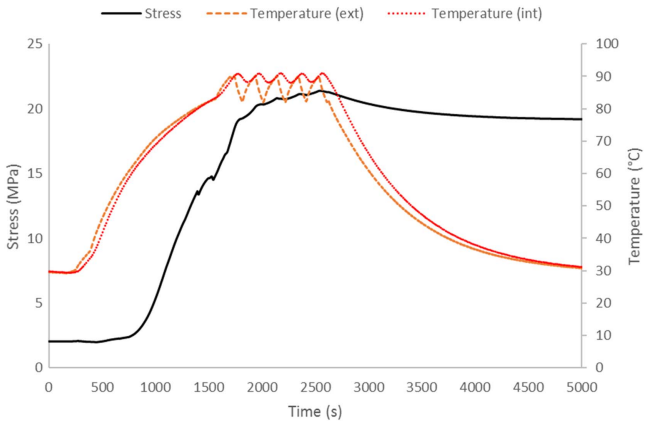


**Figure 11.** Restrained shrinkage stress test on PET tendon—test 1.

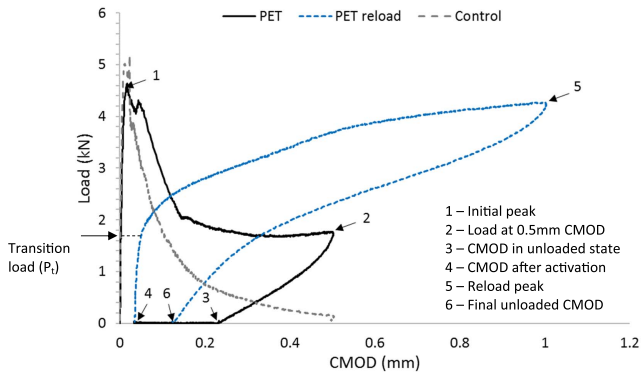


**Figure 12.** Load-CMOD curves for unreinforced test and control beams—typical graph.

post-processed in the DaVis software to track movement over time, generating 2D strain images to visualise crack closure.

## 5. Results and discussion

### *5.1. Polymer tendon shrinkage stress*

Figure 11 shows the graph of stress and temperature against time from the restrained shrinkage stress test 1 on the PET tendons. This is typical of all of the tests undertaken. Table 4 shows the peak and final restrained shrinkage stress values for all three tendons. The final stress is defined as the stress at 30 °C after cooling.

In all three tests, as the temperature was raised above $T_g$ (60 °C–80 °C) the restrained shrinkage stress rapidly increased, up to a maximum of 19.93–21.39 MPa after 15 min at 90 °C. Upon cooling, there was a gradual drop in shrinkage stress, attributed to a decrease in the entropic state of the molecular chains, resulting in a final stress plateau at between 17.76 and 19.19 MPa. The coefficient of variation for both the peak and final stress, shown in table 4, was 3.2% and 3.6% respectively. The method of manufacture therefore produces repeatable peak and final stresses in the manufactured tendons.

**Table 4.** Peak and final restrained shrinkage stress results from PET tendon tests.

| Test | Peak stress (MPa) | Final stress (MPa) | CoV peak (%) | CoV final (%) |
|---|---|---|---|---|
| 1 | 21.39 | 19.19 | | |
| 2 | 19.93 | 17.83 | 3.2 | 3.6 |
| 3 | 20.11 | 17.76 | | |

**Table 5.** Compressive strength results from cube samples (average of 3 cubes).

| Age (days) | Compressive strength (N mm$^{-2}$) | CoV (%) |
|---|---|---|
| 7 | 36.96 | 2.35 |
| 28 | 51.17 | 0.55 |

### *5.2. Compressive strength and consistency class*

Table 5 shows the compressive strength results from the cube samples. All of the strength results were above the target characteristic compressive strength of 45 N mm$^{-2}$, with a mean value exceeding 49 N mm$^{-2}$. The mix therefore conforms to the strength class C35/45 based on EN 206:2013 in terms of both strength and variability. The measured slump of the mix was 150 mm, falling into consistency class S3 (BSI 2013).

### *5.3. Unreinforced beams*

Figure 12 shows typical load-CMOD curves for the unreinforced test and control samples and figure 13 the computed stress distribution diagrams at various stages of the experiment. These were computed assuming that concrete is a no-tension material, Engineering Beam theory is applicable and that the tendon is unbonded between anchorages. Comparing the initial loading peaks (point 1) gives an average reduction

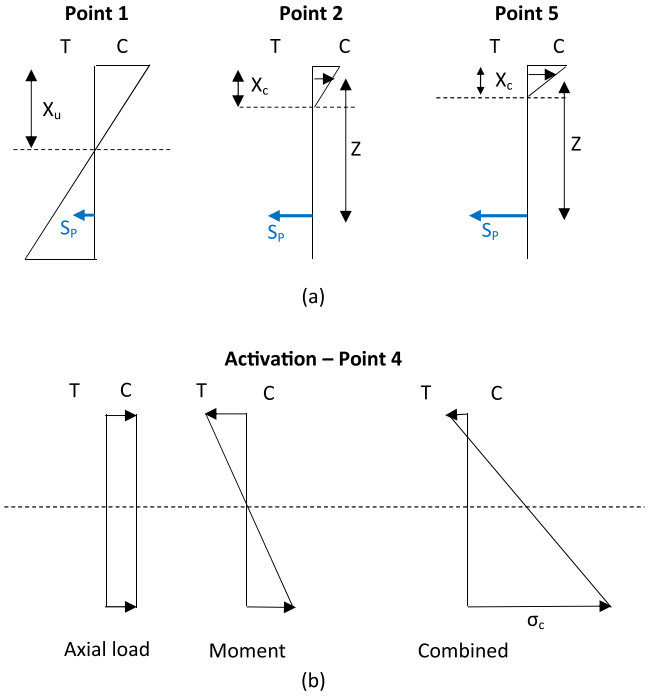


**Figure 13.** Stress block diagrams for (a) points 1, 2 and 5 on figure 4.35; (b) activation of the polymer tendon (point 4 on figure 4.35). T = tension, C = compression, SP = Stress applied to polymer tendon, Xu = depth of neutral axis (un-cracked section), Xc = depth of neutral axis (cracked section), $F_P$ = shrinkage force applied by the polymer.

in peak load of 6.2% for the PET samples (4.78 kN compared to 5.10 kN for the controls), attributed to the replacement of concrete with the PET filament tendon, which take up approximately 1.8% of the cross-sectional area. As illustrated by figure 13, at point 1 the un-cracked concrete is assumed to be linear elastic and the polymer tendon to be subject to stress $S_{P1}$, which is the stress associated with its elongation between anchor points at this load level. This results in a stress of 0.5 N mm$^{-2}$ in the polymer for the typical sample shown in figure 12.

The shape of the response diagram between points 1 and 2 results from a loss of stiffness due to concrete cracking and an increase in the tendon force, the latter being caused by the extension of the tendon between anchor points due to the overall increase in flexural displacements of the beam.

Assuming that concrete carries no-tension after cracking initiates, the stress distribution at point 2 may be assumed to be that shown in figure 13(a). Using the idealised model, the stress in the polymer at this load point may be calculated as follows;

$$S_{P2} = \frac{M_2}{Z \cdot A_P}, \quad (1)$$

where $M$ is the applied moment, $Z$ is the lever arm, $A_P$ is the area of the polymer and the numbered subscript denotes the loading point.

With an applied load of 1.77 kN (for the typical graph shown), $S_{P2}$ is 21.6 N mm$^{-2}$. From previous experiments detailed within Teall *et al* (2017), this is known to be well within the polymer's elastic zone.

Upon unloading (point 3), a residual CMOD of 0.195 mm to 0.231 mm was recorded. Such residual displacements are typical in concrete fracture tests and are normally attributed to a mismatch of asperities and local friction between opposing crack faces(van Mier 1996). The fact that the residual CMOD of the PET beam is significantly lower than that of the control sample in figure 12 is due to the load in the tendon at this point (induced from tendon extension via the residual crack opening), which exerts an eccentric compressive load to the beam that acts to close the crack. It is also noted that the loading rig was only capable of applying downward vertical forces to the beam, which provides zero the lower bound for P shown in figure 12.

Upon activation (point 3 to point 4), the compressive stress produced by the tendon caused a reduction in CMOD, as the crack faces were drawn back together. Figure 13 shows the idealised stress profile of the beam at this stage, which is made up of the stresses due to the applied axial load and moment from the tendon, it being assumed the beam can accommodate nominal tensile stresses in the upper part of the beam. Table 6 shows the percentage crack closure of each of the test samples. This closure was measured both by the change in CMOD readings and from microscope measurements of the induced crack before and after the activation process. The recorded CMOD values were larger than the microscope measurements due to the position of the gauge, approximately 4 mm below the bottom surface of the beam. The difference between the two measurements was 0.035–0.063 mm before activation, reducing to 0–0.007 mm after activation as the crack faces were pulled back together. The variation in measurements between beams is caused by differing crack width, variations in actual notch depth and variation in the exact position of microscope measurements relative to the CMOD gauge.

The reduction in difference between measurements upon activation is due to a decrease in beam curvature caused by the compressive force from the tendon. It is therefore to be expected that the crack closure measured by change in CMOD will be slightly higher than those measured by microscope images.

Activation of the polymer tendon significantly increased the stiffness of the beams. This is shown by the reload curve (point 4 to point 5) in figure 12, which has two phases: (i) the initial steep portion of the curve that relates to the stiffness of the beam with a closed crack; and (ii) the subsequent non-linear section of the curve that reflects a gradual reduction in stiffness due to the opening and further extension of the crack. The start of phase two, denoted the 'transition load' in figure 12, may be associated with the point at which the bending stress in the bottom fibre of the beam overcomes the corresponding compressive stress from the tendon i.e. the point at which the crack starts to re-open.

At point 5, the stress applied to the polymer $S_P$ can again be calculated from equation (1), using $M$, $x_c$ and $Z$ values appropriate to point 5. With an applied load of 4.27 kN, $S_P$ is equal to 52.1 N mm$^{-2}$. This is still well within the elastic zone

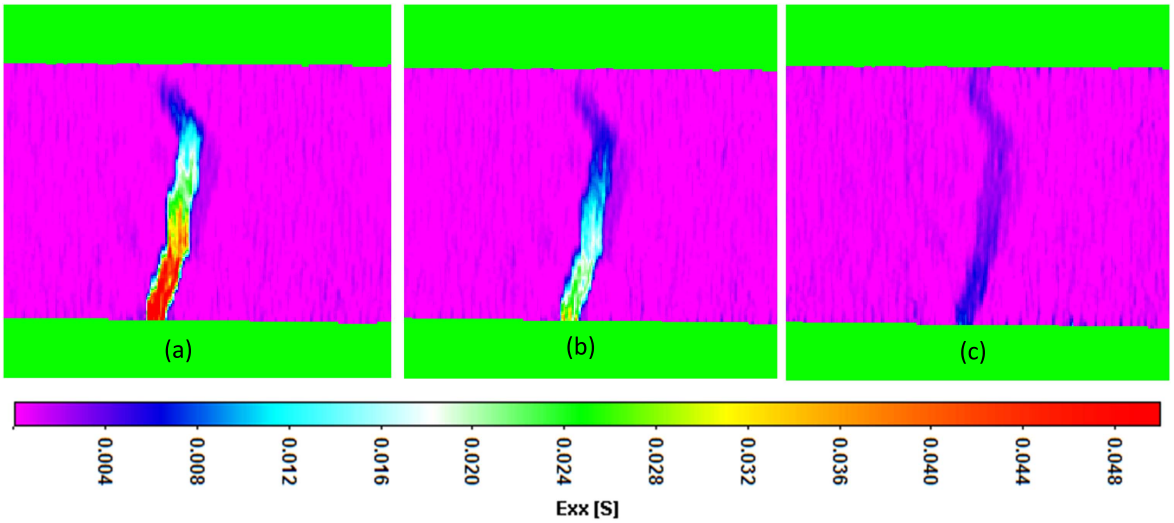


**Figure 14.** Digital image correlation (DIC) camera snapshots showing closure of concrete crack using PET tendons. Axis indicates strain. (a) Loaded to 0.5 mm CMOD; (b) unloaded; (c) post-activation.

**Table 6.** Crack closure of unreinforced beams by PET tendon activation.

| Sample | CMOD before (mm) | CMOD after (mm) | CMOD closure (%) | Microscope before (mm) | Microscope after (mm) | Microscope closure (%) |
|---|---|---|---|---|---|---|
| PET A | 0.231 | 0.035 | **85** | 0.169 | 0.028 | **83** |
| PET B | 0.195 | 0.045 | **77** | 0.132 | 0.045 | **66** |
| PET C | 0.2 | 0.060 | **70** | 0.165 | [a] | |

[a] Measurement not taken due to equipment error.

**Table 7.** Restrained shrinkage stress of polymer tendons within beams—calculated values.

| Sample | Polymer compressive load (kN) | Calculated polymer restrained shrinkage stress (MPa) | CoV (%) |
|---|---|---|---|
| PET A | 1.7 | 19.71 | |
| PET B | 1.3 | 15.1 | 11.5 |
| PET C | 1.4 | 16.23 | |

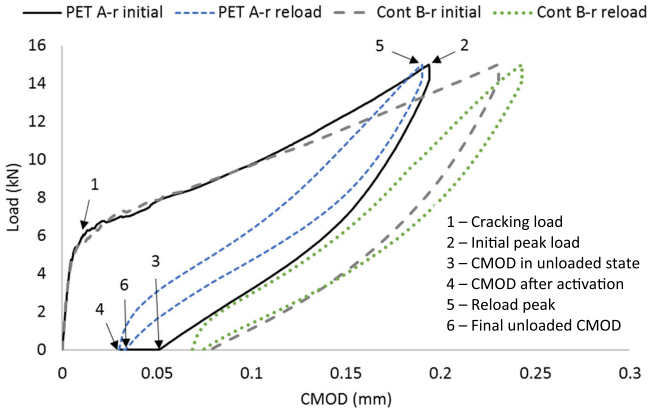


**Figure 15.** Load-CMOD curves for PET A-r and CONT B-r samples.

of the polymer, so it can be assumed that yielding has not occurred.

Upon unloading (point 6), the CMOD did not return to its value after activation (point 4), which can again be attributed to increased misalignment between crack faces during the second phase of cracking.

The results indicate that the compressive stress produced by the tendons was sufficient to close the induced crack width by up to 85%. This crack closure is also shown by the strain images in figure 14 produced by the DIC camera system.

The restrained shrinkage stress generated by the polymer tendons inside the beams was calculated from the reload curves (point 4 to point 5 on figure 12) of the PET beams after activation.

The transition load that occurs between load points 4 and 5 is used to compute an estimate of the activated tendon stress by assuming that the extension of the tendon due to beam flexure is negligible at this point and that the compressive stress in the bottom fibre of the beam caused by the pre-stress exactly balances the bending stress from the applied moment. This condition is expressed mathematically in equation (2).

$$0 = \frac{\sigma_p \cdot A_p}{A_u} + \frac{\sigma_p \cdot A_p \cdot e \cdot y}{I_u} + \frac{M_t \cdot y}{I_u} \qquad (2)$$

in which $M_t$ is the mid-span moment associated with the applied 'transition load' $P_t$ and subscript u denotes un-cracked properties

**Table 8.** Crack displacements and closure from CMOD and microscope measurements (in mm)—microscope measurements are an average over both sides of the beam samples.

| | PET A-r | | PET B-r | | PET C-r | | CONT A-r | | CONT B-r | | CONT C-r | |
|---|---|---|---|---|---|---|---|---|---|---|---|---|
| | CMOD | Micro. | CMOD | Micro. | CMOD | Micro. | CMOD | Micro. | CMOD | Micro. | CMOD | Micro. |
| Peak load | 0.194 | 0.120 | 0.217 | 0.126 | 0.196 | 0.120 | 0.246 | 0.168 | 0.231 | 0.132 | 0.201 | 0.126 |
| Unloaded | 0.050 | 0.023 | 0.064 | 0.028 | 0.063 | 0.021 | 0.080 | 0.043 | 0.077 | 0.032 | 0.059 | 0.024 |
| Activated | 0.030 | 0.014 | 0.048 | 0.021 | 0.047 | 0.019 | — | — | 0.069[a] | 0.028 | — | — |
| Crack closure | 0.019 | 0.009 | 0.017 | 0.007 | 0.016 | 0.002 | — | — | 0.008 | 0.004 | — | — |
| Crack closure (%) | **39%** | **39%** | **26%** | **25%** | **26%** | **10%** | — | — | **11%** | **13%** | — | — |

[a] CONT B-r left for an hour following unloading, closure due to elastic effect of steel reinforcement.

**Table 9.** Maximum recorded temperatures during activation.

| | PET A-r | | | PET B-r | | | PET C-r | | |
|---|---|---|---|---|---|---|---|---|---|
| Thermocouple | External | Internal | Wire | External | Internal | Wire | External | Internal | Wire |
| Temperature (°C) | 82.7 | 84.6 | 135.8 | 60.8 | 74.2 | 147.0 | 59.2 | 68.1 | 150.0 |

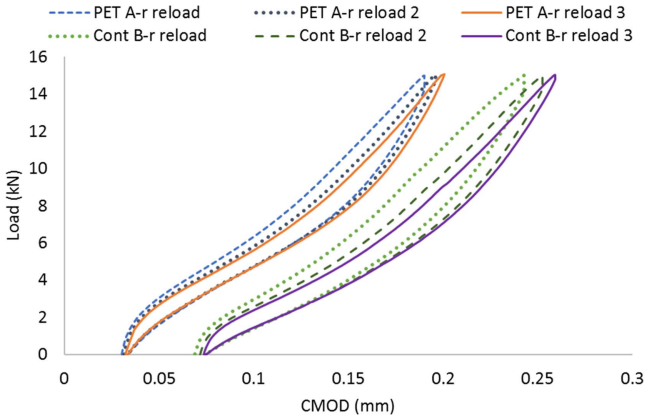


**Figure 16.** Load-CMOD reload curves for PET A-r and CONT B-r.

Table 7 shows the calculated restrained shrinkage stress values for the three PET samples using this method.

The calculated values are similar to the final stress values observed in the tendon experiments undertaken outside of concrete beams, given in table 4. PET B and C exhibited lower shrinkage stress results than PET A, which agrees with the lower percentage of crack closure observed in table 6. The coefficient of variance of 11.5% within the beam samples compared to 3.6% outside indicates increased variability of results when activating the tendons inside concrete. The concrete beam arrangements add several new variables, including the eccentricity of the tendons and any expansion and contraction of the concrete, which affect the final shrinkage stress observed from the tendons.

### *5.4. Reinforced beams*

Figure 15 shows the load-CMOD curve for the PET A-r test beam compared to CONT B-r. This control sample was used for comparison as it was left for an hour following loading to investigate the effect of the steel reinforcement in closing the crack over time.

The inclusion of the un-activated PET tendon had no noticeable impact on the load at which concrete cracking took place (point 1). However, there is an apparent increase in overall stiffness of the PET beam prior to activation as shown by a reduced CMOD reading at the maximum load of 15 kN (point 2). On average, the CMOD of the PET beams at 15 kN before activation was 10.6% lower than the control beams (0.202 mm compared to 0.226 mm).

Upon activation (point 3 to point 4), the CMOD reduced by between 26% and 39% for the PET beams, compared to an 11% reduction due to the action of the steel in CONT B-r when left for an hour after loading. The microscope measurements show very similar results, with 25%–39% closure in PET A-r and PET B-r samples compared to 13% in CONT B-r. Table 8 shows the crack closure upon activation for all beams based on the CMOD and microscope measurements. A notable exception is PET C-r which shows only 10% closure based on microscope measurements compared to 26% based on CMOD. The reason for this discrepancy is unclear, although the residual crack width measured from microscope images in this sample were the smallest of all samples, making changes in crack width more difficult to measure.

The reload curve following activation of PET A-r (point 4 to point 5 in figure 15) again shows an apparent increase in stiffness, as the CMOD at 15 kN load reduced from 0.194 mm to 0.190 mm. In contrast, the CMOD of CONT B-r at 15 kN was 0.243 mm upon reloading, an increase from 0.231 mm on initial loading.

There appeared to be some interference with the electrical activation system by the steel reinforcement. It is suggested that this may be due to induced current in the steel running parallel to the heating coils. The target internal thermocouple temperature of 90 °C was not achieved in any of the reinforced samples, even when the temperature on the heating wire was raised to 150 °C. The wire temperature was not increased beyond this point to avoid locally melting the

**Table 10.** CMOD and microscope crack measurements on reload cycles for all samples (mm unless stated).

| | PET A-r | | PET B-r | | PET C-r | | CONT A-r | | CONT B-r | | CONT C-r | |
|---|---|---|---|---|---|---|---|---|---|---|---|---|
| | CMOD | Micro. | CMOD | Micro. | CMOD | Micro. | CMOD | Micro. | CMOD | Micro. | CMOD | Micro. |
| R1 peak | 0.190 | 0.108 | 0.223 | 0.118 | 0.204 | 0.114 | 0.263 | 0.173 | 0.243 | 0.168 | 0.215 | 0.140 |
| R1 unload | 0.032 | 0.012 | 0.052 | 0.024 | 0.050 | 0.018 | 0.079 | 0.047 | 0.074 | 0.038 | 0.061 | 0.035 |
| R2 peak | 0.196 | | 0.229 | | 0.213 | | 0.274 | | 0.252 | | | |
| R2 unload | 0.033 | | 0.052 | | 0.050 | | 0.080 | | 0.074 | | | |
| R3 peak | 0.199 | | 0.232 | | 0.216 | | | | 0.259 | | | |
| R3 unload | 0.034 | | 0.052 | | 0.050 | | | | 0.074 | | | |
| Increase over 3 cycles | 4.7% | | 4.0% | | 5.9% | | | | 6.6% | | | |

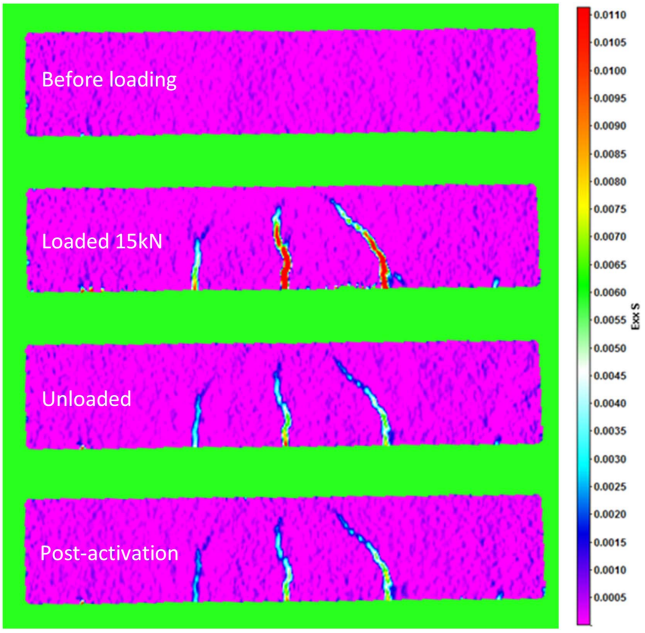


(a)

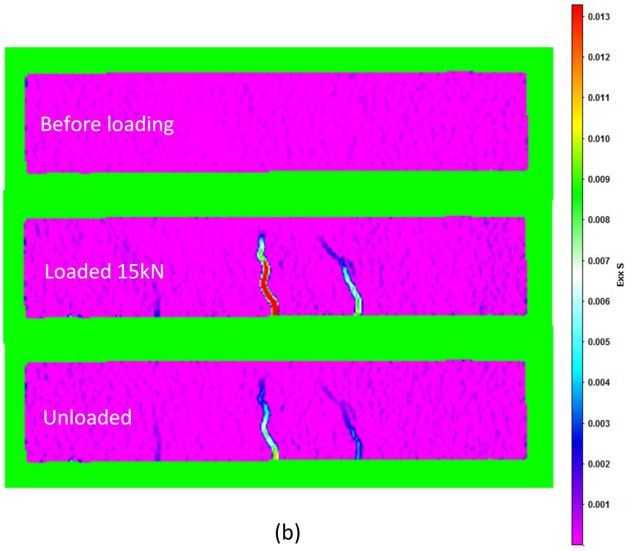


(b)

**Figure 17.** Digital image correlation (DIC) snapshots (a) activation of tendon in PET A-r (b) loading of CONT A-r. Axis indicates strain.

PET filament. The maximum recorded temperatures are shown in table 9.

A comparison of three successive reload cycles of PET A-r and CONT B-r is shown in figure 16. The CMOD and microscope measurements at peak load and after unloading for all samples are displayed in table 10. While all samples experienced increasing displacement at peak load with repeated loading, this effect was reduced in the PET samples. On average, the peak load displacement increased by 4.8% over three reload cycles for the PET beams, compared to 6.6% for CONT B-r. Moreover, the average final, unloaded CMOD reading after all load cycles for the PET beams was 0.045 mm, 39% smaller than the 0.074 mm measured on CONT B-r. Considering only PET A-r, which experienced the most successful polymer activation, this reduction in final CMOD reading increases to 54%. This suggests that the compressive stress produced by the polymer tendon can reduce gradual displacement over time due to cyclic loading and that the compressive force generated by the PET was not lost during reload cycles.

These results are similar to those produced by Yachuan and Jinping (2008) using SMA wires in their super-elastic form in concrete beams, in which deflections were recovered over repeated load cycles. However, the SMA in this form can only recover displacements, not produce a compressive stress on the crack faces required to enhance autogenous healing. An autonomic healing response was instead introduced using brittle, adhesive-filled fibres.

Figure 17 shows DIC images of the test on sample PET A-r. Three separate cracks are created by the loading process in both the PET and control beams due to the presence of the reinforcement. The cracks are still present in the sample following activation, and the crack closure is not as clear from the DIC strain images as in the unreinforced samples.

Due to the steel reinforcement, the induced cracks are much smaller in the reinforced PET samples upon unloading (average of 0.059 mm CMOD compared to 0.209 mm CMOD in unreinforced samples). In addition to the challenges of achieving 90 °C across all of the filaments during activation, the polymer tendon is also working against the misalignment

of the crack faces and any debris wedged in the crack following initial loading to achieve any crack closure. In the unreinforced samples, the residual cracks from initial loading were large enough to allow some crack closure to occur before effects of misalignment or debris could become significant.

Given the limited success of these tendons within reinforced beams, it is proposed by the authors that this SMP system may be better employed as full or partial replacement for steel reinforcement, with the tendons acting both as reinforcement and as a partial delayed prestressing system for crack width reduction. In this way, the SMP could produce a low level pre-stress on the concrete member to restrict crack widths to below the levels required by current design standards, while enhancing the autogenous healing where water is present. This approach could also reduce material costs by replacing the expensive steel bars and avoid issues with the polymer activation system interacting with the steel. It is also noted that on-going work on developing higher performance tendons and resolving some of the present activation problems should widen the range of applicability of the system in the future.

## 6. Conclusions

A shape memory PET filament tendon has been developed which can be activated via an electrical wire system to close cracks in concrete beam samples. Restrained shrinkage stress experiments performed on the polymer tendons alone produced stresses of 17.79–19.19 MPa upon activation and cooling.

Tendons embedded within unreinforced and reinforced concrete beams were cracked in three-point bending before activating the polymer using the electrical wire system. The stress produced in unreinforced beams resulted in crack closure of up to 85% and a significant increase in beam stiffness on reloading. In reinforced beams, despite challenges in achieving full activation of the polymer tendons, the measured crack closure was 26%–39% based on CMOD measurements across the largest crack. Incremental increases in CMOD during repeated loading cycles on the reinforced beams were also reduced by the polymers.

An electrically activated SMP tendon crack closure system for concrete, as described within this paper, has not previously been demonstrated. Based on the results of these experiments, it is suggested that a potential use for the SMP system may be as full or partial replacement for steel reinforcement in concrete structures.

## Acknowledgments

Thanks must go to the EPSRC for their funding of the Materials for Life (M4L) project (EP/K026631/1) and to Costain Group PLC for their industrial sponsorship of the project and author.

## ORCID iDs

Oliver Teall https://orcid.org/0000-0002-1840-3495

## References

Behl M and Lendlein A 2007 Shape-memory polymers *Mater. Today* **10** 20–8

BSI 2013 BS EN 206:2013 *Concrete—Specification, Performance, Production and Conformity* (London: British Standards Institute)

Coates P D and Ward I M 1981 Die drawing: solid phase drawing of polymers through a converging die *Polym. Eng. Sci.* **21** 612–8

De Rooij M R, van Tittelboom K, De Belie N and Schlangen E 2013 Self-healing phenomena in cement based materials *State-of-the-Art Report of RILEM* TC 221-SHC

Government H 2013 Construction 2025 *Construction 2025 Industrial Strategy: government and industry in partnership.* https://gov.uk/government/publications/construction-2025-strategy

Heide N T and Schlangen E 2007 Self-healing of early age cracks in concrete *1st Int. Conf. on Self Healing Materials* (Dordrecht: Springer)

Homma D, Mihashi H and Nishiwaki T 2009 Self-healing capability of fibre reinforced cementitious composites *J. Adv. Concr. Technol.* **7** 217–28

Isaacs B 2011 Self-healing cementitious materials *Doctor of Philosophy* Cardiff University

Isaacs B, Lark R, Jefferson T, Davies R and Dunn S 2013 Crack healing of cementitious materials using shrinkable polymer tendons *Struct. Concr.* **14** 138–47

Jefferson A, Joseph C, Lark R, Isaacs B, Dunn S and Weager B 2010 A new system for crack closure of cementitious materials using shrinkable polymers *Cement Concr. Res.* **40** 795–801

Li V C, Lim Y M and Chan Y-W 1998 Feasibility study of a passive smart self-healing cementitious composite *Composites* B **29** 819–27

Meng Q and Hu J 2009 A review of shape memory polymer composites and blends *Composites* A **40** 1661–72

Neville A M 2012 *Properties of Concrete* (Upper Saddle River, NJ: Prentice-Hall)

Schneider C A, Rasband W S and Eliceiri K W 2012 NIH Image to ImageJ: 25 years of image analysis *Nat. Meth.* **9** 671–5

Teall O, Pilegis M, Sweeney J, Gough T, Thompson G, Jefferson A, Lark R and Gardner D 2017 Development of high shrinkage polyethylene terephthalate (PET) shape memory polymer tendons for concrete crack closure *Smart Mater. Struct.* **26** 4

Van Breugel K 2007 *Is There a Market for Self-Healing Cement-Based Materials Proc. 1st Int. Conf. Self-healing Materials (Noordwijk aan Zee, The Netherlands, 18-20 April 2007)*

Van Den Heede P, Maes M and De Belie N 2014 Influence of active crack width control on the chloride penetration resistance and global warming potential of slabs made with fly ash + silica fume concrete *Constr. Build. Mater.* **67** 74–80

Van Mier J 1996 *Fracture Processes of Concrete* (Boca Raton, FL: CRC Press)

Xie T 2011 Recent advances in polymer shape memory *Polymer* **52** 4985–5000

Yachuan K and Jinping O 2008 Self-repairing performance of concrete beams strengthened using superelastic SMA wires in combination with adhesives released from hollow fibers *Smart Mater. Struct.* **17** 025020

Yang Y, Lepech M D, Yang E-H and Li V C 2009 Autogenous healing of engineered cementitious composites under wet–dry cycles *Cement Concr. Res.* **39** 382–90